JGR Atmospheres

RESEARCH ARTICLE
10.1029/2018JD030019

Key Points:
- A method of combining CrIS brightness temperature difference to its measurement noise ratio for VIIRS DCC identification is introduced
- The methodologies and technical approaches of monitoring VIIRS RSB calibrations using DCC with collocated CrIS measurements are developed
- This method can be applied to other imagers with collocated advanced infrared sounders to monitor the calibration stabilities of RSBs

Correspondence to:
J. Li,
jun.li@ssec.wisc.edu

Citation:
Gong, X., Li, Z., Li, J., Moeller, C., & Wang, W. (2019). Monitoring the VIIRS Sensor Data Records reflective solar band calibrations using DCC with collocated CrIS measurements. *Journal of Geophysical Research: Atmospheres*, *124*, 8688–8706. https://doi.org/10.1029/2018JD030019

Received 19 NOV 2018
Accepted 1 JUN 2019
Accepted article online 25 JUL 2019
Published online 7 AUG 2019

Author Contributions:
Conceptualization: Xinya Gong, Zhenglong Li, Jun Li
Data curation: Xinya Gong, Zhenglong Li
Formal analysis: Xinya Gong, Zhenglong Li
Funding acquisition: Jun Li, Christopher C. Moeller
Investigation: Xinya Gong, Zhenglong Li
Methodology: Xinya Gong, Zhenglong Li, Jun Li, Wenhui Wang
Project administration: Jun Li, Christopher C. Moeller
Resources: Xinya Gong, Zhenglong Li, Jun Li, Christopher C. Moeller
Software: Xinya Gong, Zhenglong Li
Supervision: Zhenglong Li, Jun Li, Christopher C. Moeller
(continued)

©2019. American Geophysical Union. All Rights Reserved.

Monitoring the VIIRS Sensor Data Records Reflective Solar Band Calibrations Using DCC With Collocated CrIS Measurements

Xinya Gong[1,2,3], Zhenglong Li[2], Jun Li[2], Christopher C. Moeller[2], and Wenhui Wang[4]

[1]National Satellite Meteorological Center, China Meteorological Administration, Beijing, China, [2]Cooperative Institute for Meteorological Satellite Studies, University of Wisconsin-Madison, Madison, WI, USA, [3]Key Laboratory of Radiometric Calibration and Validation for Environmental Satellites, China Meteorological Administration, Beijing, China, [4]Global Science and Technology, Inc., Laurel, MD, USA

Abstract As uniform and stable objects, deep convective clouds (DCCs) are often used to monitor the calibration stabilities of the reflective solar bands (RSBs) of the Visible Infrared Imaging Radiometer Suite (VIIRS) onboard the Suomi National Polar-orbiting Partnership. Traditionally, DCCs are identified by the legacy 11-μm brightness temperature (BT11) threshold method. With the collocated Cross-track Infrared Sounder (CrIS), a method of combining the BT difference between a water vapor absorption channel and a window channel to its measurement noise ratio (BNR) is adopted and applied to DCC identification. The BNR method improves the DCC detections over the legacy method because it is less contaminated with high clouds not thick and bright enough. Using observations from 2017 to 2018, the results show BNR has better performances than BT11 for identifying DCCs and monitoring RSBs. When comparing to BT11, BNR has more robust and invariant time series of monthly reflectance for all RSBs; that is, the standard deviation and total variation range (maximum-minimum) are up to 47% smaller. Because BNR affects more on the left tails (less reflective) than the modes of the histograms of reflectance, the improvement is more significant on the mean reflectance than the mode. BNR detects fewer DCCs than BT11, but with more confidence. This allows the weekly and daily time series for monitoring RSBs in higher temporal frequencies. This method can be applied to other imagers with collocated advanced infrared sounders for detecting DCCs and monitoring the calibration stabilities of RSBs.

1. Introduction

Onboard the Suomi National Polar-orbiting Partnership (SNPP) and the National Oceanic and Atmospheric Administration (NOAA)-20 satellites (previously Joint Polar Satellite Systems 1, or JPSS-1), the Visible Infrared Imaging Radiometer Suite (VIIRS) collects imagery and radiometric data of the Earth and its atmosphere (Cao et al., 2013; Cao et al., 2014; Hillger et al., 2013), with high radiometric accuracy and spatial resolution (750 m for moderate-resolution bands [M-bands] and 375 m for imaging-resolution bands [I-bands] at nadir). As input for more than 20 Environmental Data Records (EDR) products, such as ocean color, vegetation, aerosols, fire, cloud properties, and surface albedo (Xiong et al., 2014, 2016), it is critical to monitor the radiometric stability of VIIRS Sensor Data Records (SDR) to ensure stable performance. Among 22 VIIRS bands, the Reflective Solar Bands (RSBs) consist of 14 bands (11 M-bands and 3 I-bands) covering the spectrum of 0.4 to 2.3 μm; the RSBs use the solar diffuser (SD) data and SD Stability Monitor for calibration (Sun & Wang, 2014; Xiong et al., 2014, 2016).

Not long after SNPP launched on 28 October 2011, the radiometric sensitivities of VIIRS RSBs were found to decrease much faster than designed. Significant degradations in SD, SD Stability Monitor detectors, and the Rotating Telescope Assembly mirror have been observed since mid-2013 and early 2014 (Cao et al., 2013; Cao et al., 2014; Sun & Wang, 2014; Wolfe et al., 2013). Improved radiometric calibration procedures together with parameters have been developed and updated several times throughout the mission's lifetime. An automated procedure was implemented since December 2015 to update the coefficients for RSB calibrations once per orbit (Blonski & Cao, 2015; Cardema et al., 2012; Rausch et al., 2013; Weng et al., 2017). To further facilitate the applications of VIIRS RSBs, it is critical to assess the radiometric accuracies and calibration stabilities of those bands by independent approaches, including using the measurements

Validation: Xinya Gong, Zhenglong Li, Wenhui Wang
Visualization: Xinya Gong, Zhenglong Li
Writing - original draft: Xinya Gong
Writing – review & editing: Xinya Gong, Zhenglong Li, Jun Li, Christopher C. Moeller, Wenhui Wang

of the stable objects (Bhatt et al., 2014; Uprety & Cao, 2015; Wang & Cao, 2014, 2015, 2016) as well as the legacy instruments (Uprety et al., 2013; Wu et al., 2016).

Deep convective clouds (DCCs) are extremely cold and thick cloud systems with cloud tops near the tropopause. DCC systems reflect most visible (VIS) sunlight and absorb some solar radiation in the near-infrared (NIR). They are not notably affected by water vapor (WV) or other absorption gases in the troposphere and can be used to monitor the radiometric stabilities of the RSBs (Doelling et al., 2004; Fougnie & Bach, 2009; Hu et al., 2004; Minnis et al., 2008). As an invariant target calibration approach, DCCs have the advantage of being the brightest targets available globally. Using DCCs for RSB calibrations was first introduced by Hu et al. (2004) using the Clouds and the Earth's Radiant Energy System onboard the Tropical Rainfall Measuring Mission. The legacy method for DCC detection examines if the brightness temperature (BT) of a single infrared (IR) band of 11 micron (BT11) is smaller than a fixed BT threshold (Doelling et al., 2004; Hu et al., 2004). The DCC detection and calibration approach are further improved by incorporating additional uniform tests for both VIS and IR bands (Minnis et al., 2008) and angle restrictions (Fougnie & Bach, 2009). The improved technique requires a good VIS and IR coregistration, radiance calibration, and a dynamic range that does not saturate at DCC radiances. Thereafter, the DCC technique has been widely applied to many other sensors, such as the Medium Resolution Spectral Imager onboard FengYun-3 satellites (Chen et al., 2013), the VIIRS onboard SNPP satellites (Bhatt et al., 2014; Wang & Cao, 2014, 2015, 2016), and geostationary (GEO) sensors for intercalibration approach in the Global Space-based Inter-Calibration System (Doelling et al., 2011).

An empirical angular distribution model (ADM) developed by Hu et al. (2004) adjusts the anisotropy (radiance-flux relation) effects in the top of the atmosphere (TOA) reflectance. This ADM adjustment has been applied and demonstrated by various instruments for the VIS/NIR spectrum (Doelling et al., 2004; Doelling et al., 2013; Wang & Cao, 2015, 2016). However, it is less effective for the shortwave infrared (SWIR) spectrum partially due to solar radiation absorption by clouds (Doelling et al., 2013; Wang & Cao, 2016). Since 2012, the National Environmental Satellite, Data, and Information Service at NOAA started to provide the monthly time series of DCC reflectance at https://ncc.nesdis.noaa.gov/VIIRS/VSTS.php for VIIRS/SNPP and recently for VIIRS/NOAA-20. Previous studies showed annual cycles in the time series of monthly reflectance mean and mode for the SWIR bands (Wang & Cao, 2015, 2016). DCCs are found mostly over land during winter (December–February) in the Southern Hemisphere and mostly over ocean during summer (July–August) in the Northern Hemisphere (Bedka et al., 2018). The DCCs detected over land and ocean typically have different cluster sizes, resulting in different absorptions in the SWIR spectrum. Wang and Cao (2016) show the stability of SWIR reflectance is comparable to the natural DCC variability.

However, identifying DCC based on a fixed BT threshold is rather ambiguous. The tropical tropopause temperature varies spatially and seasonally from 193 to 212 K based on the reanalysis data sets (Aumann et al., 2006; Aumann & Ruzmaikin, 2013). The lower the BT11 threshold, the greater the chance of identifying DCCs rather than anvil conditions. However, it is at the cost of sample size. Another method for detecting DCC is based on the BT difference (BTD) between a strong WV absorption channel and a window channel (or a weak WV channel). DCCs are detected when the WV BT is warmer than the window channel due to the temperature inversion in the stratosphere (Ackerman, 1996; Schmetz et al., 1997). This method is independent of tropopause temperature and therefore is independent of the tropopause height. This method has been applied to imagers such as the Moderate Resolution Imaging Spectroradiometer and the Spinning Enhanced Visible and Infrared Imager (Setvák et al., 2007; Setvák et al., 2008), as well as hyperspectral sounders such as the Atmospheric Infrared Sounder (AIRS; Aumann et al., 2011; Aumann & Ruzmaikin, 2013). The effectiveness of BTD for DCC detection is highly related to the spectral resolution and signal-to-noise ratio of the WV band (Ai et al., 2017). One limitation of BTD method is when the BTD is close to zero. Due to observational random noises in the two IR channels, this method may mistakenly classify DCC as non-DCC or non-DCC as DCC. Note that the BT noise is larger when the BT is lower. An improved technique combining the BTD with its measurement noise ratio (BNR) is introduced by Ai et al. (2017), using either broadband imagers (e.g., the imager on the Multifunction Transport Satellite 2) or hyperspectral sounders (e.g., AIRS and the Infrared Atmospheric Sounding Interferometer; Menzel et al., 2018). BNR is an enhanced BTD method for DCC identification. However, the BTD and BNR methods cannot be applied to VIIRS directly due to the lack of WV bands.

Flown along with the VIIRS onboard SNPP, the Cross-track Infrared Sounder (CrIS; Han et al., 2013) is a Fourier transform spectrometer, providing radiance measurements of the Earth and its atmosphere at high spectral (0.625–2.5 cm^{-1}) and spatial (14 km at nadir) resolutions. The CrIS instrument has two modes of operation SDR, the nominal spectral resolution since 19 April 2012 and the full spectral resolution since 8 March 2017. In this paper, the CrIS NSR SDR data are used. Techniques have been developed to allow fast and accurate collocation of VIIRS with CrIS (Nagle & Holz, 2009; L. Wang et al., 2016). Taking advantages of high spatial resolution imaging and high spectral resolution sounding instruments from the same platform, synergistic use of collocated two types of measurements has shown to be very useful in retrieval of sounding and cloud properties (Li et al., 2004; Li et al., 2004; Li et al., 2005), and in assimilating radiances into NWP models, especially in cloudy skies (Li et al., 2005, Li et al., 2016; P. Wang et al., 2014, 2015, 2017). Previous work has pointed out the advantages of using VIIRS and CrIS for intercalibration (Chen et al., 2016, 2017; Gong et al., 2018; Moeller et al., 2013; Tobin et al., 2013; L. Wang et al., 2012). With collocated CrIS measurements, the BNR technique can be adopted and applied for detecting VIIRS DCC pixels. This study will compare the BNR method with the legacy BT11 and BTD methods for DCC identification.

CrIS onboard SNPP is a well-calibrated instrument (Han et al., 2013; Zavyalov et al., 2011; Zhou et al., 2016), with noise below specification (Zavyalov et al., 2013), high spectral and radiometric accuracy (Strow et al., 2013; Tobin et al., 2013; L. Wang et al., 2015), and high geolocation accuracy (L. Wang et al., 2013; L. Wang et al., 2017). With its long-term stability (Chen et al., 2016, 2017; Han et al., 2013; Moeller et al., 2013; Strow et al., 2013; Tobin et al., 2013; Zavyalov et al., 2013; Zhou et al., 2016), CrIS radiances are used to identify DCCs and help monitor the calibration stabilities of the VIIRS RSBs. This study provides a chance to better understand the VIIRS RSB radiometric stabilities, using the collocated infrared sounder instrument for detecting more confident DCCs. Additionally, while previous studies with the legacy BT11 method only focus on the time series of monthly or semimonthly reflectance mean and mode for monitoring the VIIRS RSBs (Wang & Cao, 2014, 2015, 2016), this study explores the daily and weekly time series as well. Furthermore, this knowledge will help identify problems in the future if abnormal issues are observed in the VIIRS SDRs.

In this paper, the data are described in section 2; the methodologies for identifying DCC is presented in section 3; the process and results of monitoring VIIRS RSBs using the CrIS based DCC techniques are presented in section 4; the summary and discussion are given in section 5.

2. Data

In this study, the radiance and geolocation data of the CrIS NSR SDR, the TOA radiance, reflectance, and geolocation data of the VIIRS SDRs from 1 January 2017 to 31 December 2018 are used for analysis. The VIIRS gridded cell-level cloud EDRs (6-km spatial resolution) are used for case demonstration. The data are restricted in the tropical regions between 25°S to 25°N. The CrIS and VIIRS SDRs are downloaded from the Comprehensive Large Array-data Stewardship System of NOAA (https://www.class.ngdc.noaa.gov). Both CrIS and VIIRS SDR processing software have been stable since March 2014, according to SDR ATBD and SDR user guides at STAR JPSS website (https://www.star.nesdis.noaa.gov/JPSS/Docs.php#S725608). And the CrIS and VIIRS SDR Validated Maturities have been reached as of the Mx8.2 and Mx8.3 installations. The VIIRS Cloud EDRs provided by the Comprehensive Large Array-data Stewardship System website are of the Provisional level quality (currently Mx8.5).

Figure 1 shows the spectral response functions of 13 VIIRS spectral bands subjected to the DCC study, including VIS/NIR bands M01–M07 (M06 is excluded due to saturation over DCCs), I01–I02, and SWIR bands M08–M11 and I03. The VIIRS thermal emissive band M15 (10.763 μm) is used for the legacy BT11 DCC detection method. Table 1 summarizes the center wavelength (or wave number), spatial resolution, and the radiometric characteristics of 13 VIIRS RSBs, as well as 2 CrIS channels at 1,231 and 1,419 cm^{-1}. In clear-sky conditions, 1,231 cm^{-1} is a very clean window channel, and 1,419 cm^{-1} is a very strong WV absorption channel peaking around the tropopause. Those two CrIS channels are used by the BTD and BNR methods for DCC detection (Ai et al., 2017; Aumann & Ruzmaikin, 2013). The noise-equivalent differential temperature (NEdT) is estimated at a scene temperature of 205 K for VIIRS M15 using the equation NEdN = dR/dT * NEdT, where dR/dT is the derivative of Planck radiance with respect to temperature and NEdN is mean noise-equivalent differential radiance of the 8 CrIS fields of view (FOVs; FOV 7 is

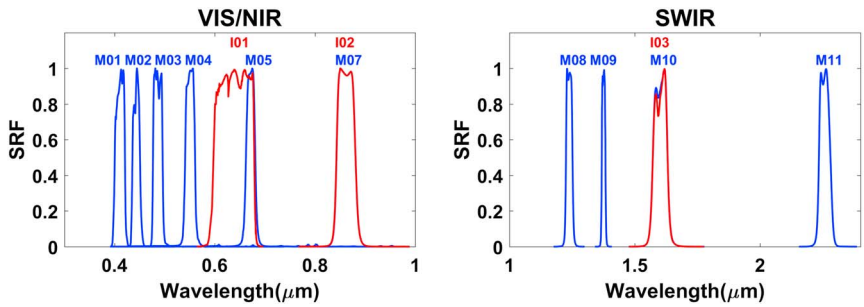

Figure 1. The spectral response functions of Visible Infrared Imaging Radiometer Suite VIS/NIR bands M01–M07 (M06 is excluded due to saturation over DCCs), I01–I02, and SWIR bands M08–M11, I03. VIS = visible; NIR = near-infrared; SWIR = shortwave infrared; SRF = spectral response function.

excluded due to larger noise) provided by Tobin et al. (2013). Unlike NEdN, which is considered scene independent, NEdT is highly dependent on scene temperature due to the nonlinearity of the Planck function. As scene temperature decreases, NEdT increases. Note that the CrIS NEdN is very stable (Chen et al., 2016; Han et al., 2013; Strow et al., 2013; Tobin et al., 2013; Zavyalov et al., 2013; Zhou et al., 2016).

It has been demonstrated that DCC reflectance is sensitive to the spatial resolution and cluster scale (Wang & Cao, 2015). To avoid inconsistency, the TOA reflectance of I-bands I01–I03 (375 m) are spatially averaged to M-band grids (750 m). As all the TOA reflectance is converted to M-band grids, VIIRS M15 (10.763 μm) is used as an example of the legacy BT11 method for identifying DCCs and monitoring VIIRS RSB reflectance in the following discussions.

3. Methodologies for DCC Detection

3.1. VIIRS/CrIS Collocation

Using the imager/sounder collocation tool developed by the Atmosphere Science Investigator-led Processing Systems team at SSEC (Nagle & Holz, 2009), the row/column indices, and weights of VIIRS pixels that fall within each CrIS FOV are calculated. Depending on the local zenith angle (LZA) and location, each CrIS FOV sees about 500 (nadir) to 1,200 (scan edge) collocated VIIRS pixels. For monitoring RSBs, the DCC data

Table 1
The Center Wavelength or Wave Number, Spatial Resolution at Nadir, and the Radiometric Characteristics of the Selected VIIRS and CrIS Bands Are Summarized

		Center wavelength/wave number	Spatial resolution (nadir)	On-orbit SNR or NEdT
VIIRS VIS/NIR	M01	0.412 μm	750 m	1,045
	M02	0.445 μm		1,010
	M03	0.488 μm		988
	M04	0.555 μm		856
	M05	0.672 μm		631
	M07	0.865 μm		631
	I01	0.640 μm	375 m	214
	I02	0.865 μm		264
VIIRS SWIR	M08	1.240 μm	750 m	221
	M09	1.378 μm		227
	M10	1.610 μm		586
	M11	2.250 μm		22
	I03	1.610 μm	375 m	149
VIIRS TEB	M15	10.763 μm	750 m	0.10 K
CrIS	731	1,231 cm^{-1}	14 km	0.94 K
	881	1,419 cm^{-1}		1.49 K

Note. VIIRS = Visible Infrared Imaging Radiometer Suite; CrIS = Cross-track Infrared Sounder; VIS = visible; NIR = near-infrared; SWIR = shortwave infrared; TEB = thermal emissive band; SNR = signal-to-noise ratio; NEdT = noise-equivalent differential temperature. The spectral and on-orbit SNR is given at Low Gain Stage. The NEdT is estimated at a scene temperature of 205 K.

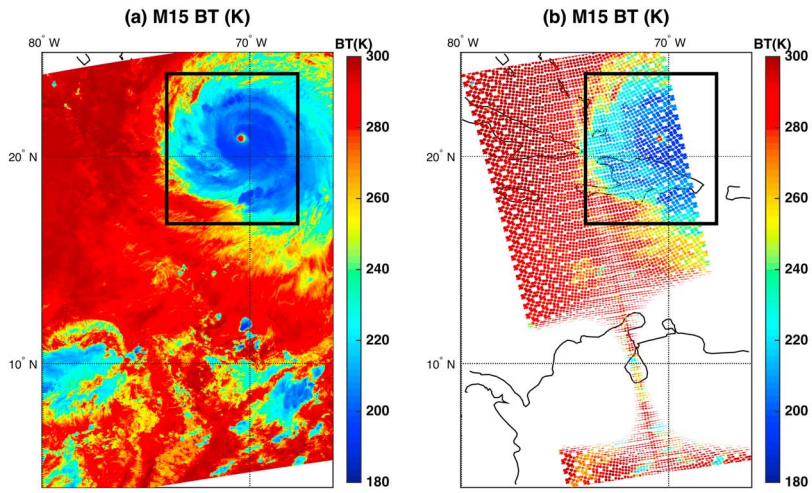

Figure 2. The Visible Infrared Imaging Radiometer Suite M15 brightness temperature (BT; K) (a) before and (b) after collocation and viewing geometry restrictions, observing Hurricane Irma at 1804 UTC on 7 September 2017. The holes after the collocation are due to the data gaps between Cross-track Infrared Sounder fields of view. The blank area around 10°N latitude is due to relative azimuth angles larger than 170° or smaller than 10°. The pixels at the scan edges with local zenith angles larger than 35° or solar zenith angle larger than 40° are excluded. The black box outlines the hurricane area shown in Figure 3.

sets are constructed with restrictions on the viewing geometries as follows: (1) the solar zenith angle is less than 40°; (2) the LZA is less than 35°, to avoid the bow-tie effect for large zenith angles; (3) the relative azimuth angle is between 10° and 170°, to avoid the sun glint effect; and (4) the latitude is between 25°S and 25°N.

The CrIS geolocation errors reported by L. Wang et al. (2017) are not corrected in this study for three reasons. (1) The DCC detection is restricted to LZAs less than 35°, where the geolocation errors are not as significant as with larger LZAs. (2) The correction algorithm has been implemented in the operational SDR algorithm since June 2017. So while the first half of the year 2017 is not corrected, the second half is corrected. However, as will be shown later, there is no obvious difference in daily and weekly time series before and after the correction. And (3) all three methods are accompanied by a uniform test to throw away inhomogeneous scenes, which are more affected by the CrIS geolocation errors.

Figure 2 shows the VIIRS M15 BT (K) of one VIIRS granule (5-min data) observing Hurricane Irma passing the Caribbean region in Atlantic Ocean at 1804 UTC on 7 September 2017, both (a) before and (b) after collocation and viewing geometry restrictions. The data are restricted in the tropical regions between 25°S to 25°N. The holes after the collocation are due to the data gaps between CrIS FOVs. The blank area around 10°N latitude is due to relative azimuth angles larger than 170° or smaller than 10°. The pixels at the scan edges with an LZA larger than 35° or solar zenith angle larger than 40° are excluded. The black box outlines the hurricane area shown in Figure 3.

3.2. BT11 Threshold Method

Traditionally, a DCC is identified as a very cold and thick cloud system with its cloud top at or above the tropopause. A single IR window channel BT (i.e., the legacy BT11 method) lower than a fixed BT threshold can be used to detect DCCs along with some uniform tests. In this study, a technique for detecting DCCs and monitoring VIIRS RSBs like previous studies is used for comparison (Wang & Cao, 2014, 2015, 2016). The criteria for the BT11 threshold method are summarized as follows: (1) The VIIRS M15 BT (10.763 μm) is less than 205 K; (2) the standard deviation (STD) of M15 BT of the subject pixel and eight adjacent pixels is less than 1 K; (3) the STD of TOA reflectance of the subject pixel and eight adjacent pixels is less than 3% relative to the mean reflectance of the nine pixels; and (4) the four viewing geometry restrictions. However, as mentioned before, the BT11 method could be problematic because the tropopause does not have a fixed height and temperature (Aumann et al., 2006; Aumann & Ruzmaikin, 2013). Chances are a fixed BT threshold would underestimate DCCs in some areas while overestimating in others.

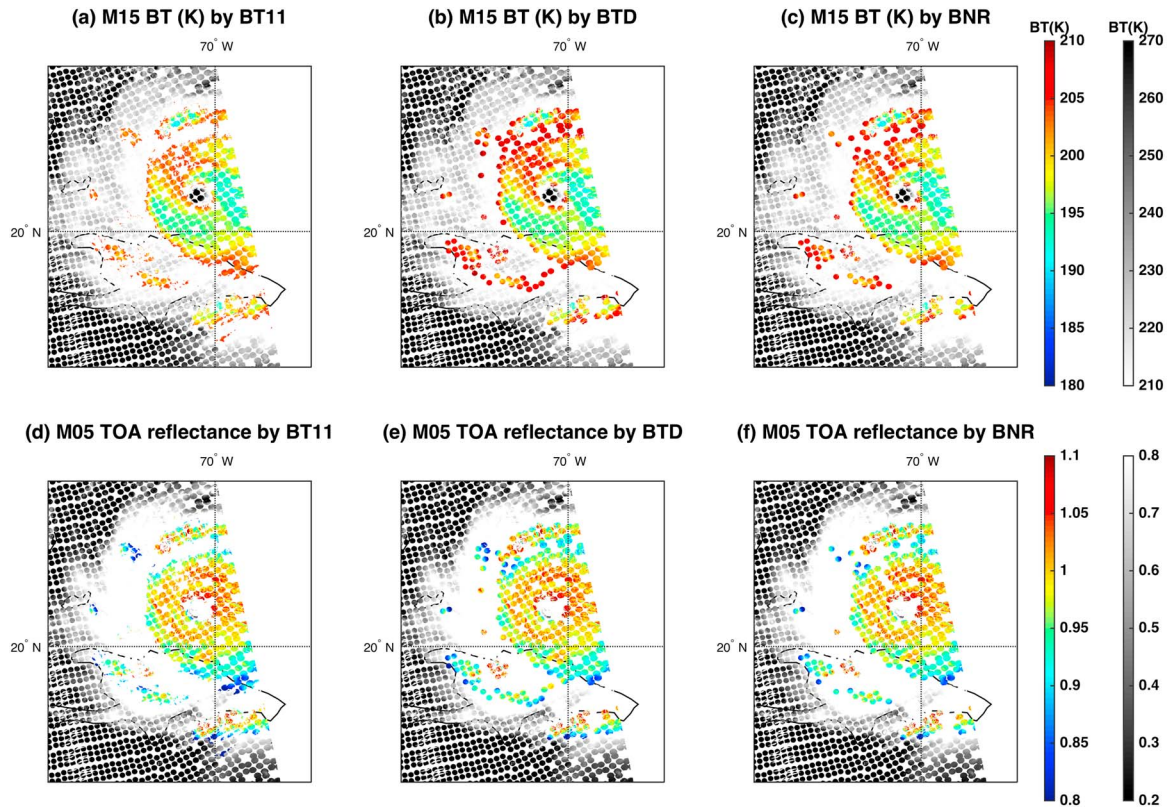

Figure 3. Visible Infrared Imaging Radiometer Suite (VIIRS) M15 brightness temperature (BT; K) of deep convective clouds (DCCs) in color selected by (a) 11-μm brightness temperature (BT11), (b) brightness temperature difference (BTD), and (c) measurement noise ratio (BNR) methods, and VIIRS M05 top-of-the-atmosphere (TOA) reflectance of DCCs selected by (d) BT11, (e) BTD, and (f) BNR methods, of Hurricane Irma at 1804 UTC on 7 September 2017, outlined by the black box in Figure 2b. The non-DCC pixels are shown in the background. The DCC yields for BT11, BTD, and BNR methods are 73,402, 85,393, and 76,074, respectively. Note that only those VIIRS pixels collocated with Cross-track Infrared Sounder are shown in this case, in order to obtain consistent results.

3.3. BTD and BNR Method

As noted by Aumann and Ruzmaikin (2013) for AIRS, 1,419 cm^{-1} is a very strong WV absorption channel peaking near 12-km altitude under cloud-free tropical conditions, and 1,231 cm^{-1} is a very clean window channel. The BTD index is defined as the BT difference between the two channels of 1,419 and 1,231 cm^{-1}. Under clear-sky or non-DCC cloudy conditions, 1,419 cm^{-1} should be colder than 1,231 cm^{-1} because it peaks much higher in the troposphere. Over DCCs, both channels see the cloud top as the main contributor. Due to strong WV absorption, 1,419 cm^{-1} should have a substantially higher contribution from the WV emission above the cloud top than 1,231 cm^{-1}. Given that temperature increases with height in the stratosphere, it is reasonable to see 1,419 cm^{-1} with a higher BT than 1,231 cm^{-1} over DCCs. Historically, clouds with a WV BT higher than the window BT were characterized as overshoots over the tropopause (Ackerman, 1996; Aumann et al., 2011; Aumann & Ruzmaikin, 2013; Schmetz et al., 1997). This BTD technique works for most cases but might be problematic when the differences between the two channels are smaller than or comparable to the observational noises. Ai et al. (2017) enhanced the BTD method for DCC detection by introducing a BNR index as the ratio between BTD and the observational noise:

$$\mathrm{BNR} = (\mathrm{BT1}-\mathrm{BT2})/\sqrt{\mathrm{NEdT1}^2 + \mathrm{NEdT2}^2}.$$

The BT1 and BT2 are the BTs of channel 1,419 and 1,231 cm^{-1}, and NEdT1 and NEdT2 are the NEdT of those two channels. The equation above indicates that BNR is the BTD method scaled by the combined noise of the two channels. This scaling is needed because (1) NEdT is already quite large for these two channels at a scene temperature of 205 K (Table 1), and (2) NEdT increases nonlinearly with decreasing scene temperatures, especially under extremely cold cloudy conditions, where DCCs are. For a given threshold, a BNR value

larger than the threshold indicates a possible DCC. When the threshold is set as zero, BNR becomes BTD. For BNR, the threshold is set as 1. This will effectively remove detections potentially affected by noise contamination. As a result, BNR detects slightly fewer DCCs but with more confidence than the BTD method. As will be shown later, even with fewer but more confident DCCs detected, the reflectance time series are more stable than those from the BT11 method. The larger the BNR threshold is, the more confidently DCCs are detected.

Given that CrIS has a spatial resolution of 14 km at nadir, within a CrIS FOV classified as DCC, it is possible that some VIIRS pixels are non-DCC. Therefore, additional uniformity tests for both IR and VIS bands are added to eliminate those suspicious pixels. The criteria for the BTD and BNR methods are summarized as follows: (1) BNR > 1 or BTD > 0; (2–7) the same criteria of uniformity tests and viewing geometry restrictions as the BT11 threshold methods are applied.

3.4. A Case Demonstration for DCC Detection

It is difficult to validate DCC detection because of the lack of truth (true knowledge whether a pixel is DCC or not). Common practice is to look at the statistics of RSB reflectance; higher and more invariant reflectance indicates a better DCC detection, because DCCs are stable objects and have near Lambertian reflectance (Doelling et al., 2004; Hu et al., 2004). Another way to determine a DCC is to look at the cloud products, such as cloud top height (CTH) and cloud optical thickness (COT). A DCC should have a large CTH (i.e., greater than 14 km) and large COT (i.e., greater than 50). In this section, a case from Hurricane Irma (2017), outlined by the black box in Figure 2b, will be used to demonstrate the advantage of BNR over the BT11 and BTD methods for DCC detection.

Figure 3 shows the VIIRS M15 BT and M05 TOA reflectance of DCCs classified by the three methods of BT11, BTD, and BNR. In Figure 3, M15 (10.763 μm) is chosen because it is the cleanest window band on VIIRS, and M05 (0.672 μm) is chosen because it is an essential band for VIIRS Cloud EDR and cloud mask products, and one of the components (blue) for VIIRS true-color Red/Green/Blue (RGB) image (Cao et al., 2013; Xiong et al., 2014, 2016). From Figure 3, the three methods identify similar geographic distributions of DCCs for Hurricane Irma, with comparable DCC yields (73,402, 85,393, and 76,074, for BT11, BTD, and BNR, respectively). Note that only those VIIRS pixels collocated with CrIS are shown in this case, in order to obtain consistent results. However, there are some differences between the three methods, for both M15 and M05 bands. For example, both BTD and BNR have a decent percentage of pixels with M15 BT larger than 205 K (i.e., northwest of the hurricane eye, Haiti, and the western Dominican Republic). These pixels are over a very uniform and dense convective overcast area and have relatively high reflectance in the solar spectrum (i.e., larger than 0.85 for M05 TOA reflectance). Since BNR uses a higher threshold value (one) than BTD (zero), it sees fewer pixels than BTD. Also, the BT11 method detects slightly more of the low reflectance pixels (i.e., less than 0.85 for M05 TOA reflectance) than BTD or BNR, although all three methods have a small percentage of those pixels. Most of those pixels are over the edge of convective cells (i.e., the south and southeast to the hurricane area).

These differences can be better seen on the histograms of VIIRS M15 BT and M05 TOA reflectance of DCC pixels classified by the three methods in Figure 4. For M15 BT less than 197 K, there are no obvious differences between the three methods. That is reasonable since clouds must be thick and high to have a M15 BT that cold. But above 197 K, BT11 detects more DCCs than BTD, and BTD more than BNR, until the BT11 threshold of 205 K. Warmer than 205 K, BTD still detects more DCCs than BNR. As a result, the DCCs selected by BTD and BNR have a little bit higher mean M15 BT than the BT11 method (199.09 K), and BTD (200.48 K) is slightly higher than BNR (199.73 K). In terms of M05 TOA reflectance, all three methods have peak reflectance in the range 0.95 to 1.0, and majority of the observations have a very bright cloud top (reflectance larger than 0.85). However, the BT11 method detects fewer DCCs among the three methods when the reflectance is larger than 0.85. For a reflectance smaller than 0.85, BNR detects the fewest DCCs, while BT11 detects the most, among the three methods. BT11 even characterizes some pixels as DCCs with reflectance lower than 0.65. As a result, BNR has the highest mean value of DCC reflectance of 0.973, compared to BT11 with 0.967 and BTD with 0.969. These results are consistent with the fact that the DCCs are very bright targets and have relatively high reflectance. Other VIS/NIR reflectance performs similarly to the M05 band.

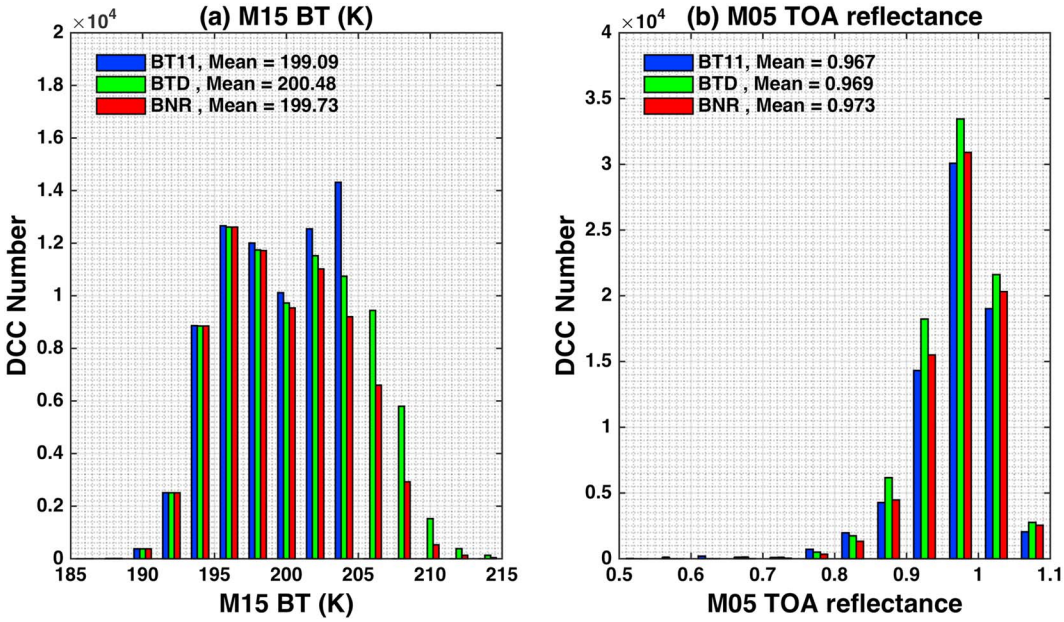

Figure 4. The histograms of (a) M15 brightness temperature (BT; K) and (b) M05 top-of-the-atmosphere (TOA) reflectance of deep convective clouds (DCCs) detected by the 11-μm brightness temperature (BT11), brightness temperature difference (BTD), and measurement noise ratio (BNR) methods. The mean values are shown in each panel.

While a lower mean M15 BT and higher mean visible reflectance indicate better DCC detection, the real questions are how to show that those pixels detected by BT11 but not by BTD or BNR are non-DCCs and that those pixels detected by BTD or BNR but not BT11 are DCCs. Meanwhile, the question of how BNR is superior to BTD needs further demonstration. For those purposes, the VIIRS pixels that see different detection results are categorized in four groups: Those detected by BT11 but missed by BTD or BNR are referred as (1) BT11/BTD/and (2) BT11/BNR/, while those detected by BTD or BNR but missed by BT11 method are referred as (3) BTD/BT11/and (4) BNR/BT11/. Figure 5 shows the histograms of VIIRS M15 BT, M05 TOA reflectance, and COT and CTH of the DCCs, for the four groups. The CTH and COT are from the VIIRS gridded cell-level cloud EDRs and matched to M-band grids. The mean value of each group is calculated for analysis and shown in each panel.

Figure 5a shows the histograms of M15 BT for the four groups. Restricting the threshold to 205 K, BT11/BTD/ and BT11/BNR/ have smaller mean M15 BT values than BTD/BT11/ and BNR/BT11/. But as will be discussed below, that does not mean BT11 detects DCCs better than BTD and BNR. Though not shown, the DCCs detected by all three methods have large mean values of COT (about 79) and CTH (about 17 km), consistent with the fact that a DCC is very thick and high cloud. However, BT11/BTD/ and BT11/BNR/have relatively flat distributions of M05 TOA reflectance with a small mean value of 0.877 (or 0.887) in Figure 5b. A substantial percentage of observations have reflectance values less than 0.8, while some have low values less than 0.65, indicating those clouds are not bright enough. This is also confirmed by the fact that the distributions of COT are quite flat in Figure 5c, with a substantial percentage of observations with COT less than 30. The mean values of COT for BT11/BTD/ and BT11/BNR/are 55.9 and 56.8, respectively, significantly smaller than the mean value of 78.6 for all the DCCs detected by the BT11 method. These results indicate that a substantial percentage of those observations detected by BT11 but missed by BTD or BNR are not thick and bright enough, which makes them less likely DCCs.

On the other hand, BTD/BT11/ and BNR/BT11/ have large mean M05 TOA reflectance values around 0.95 in Figure 5b, much higher than that of BT11/BTD/or BT11/BNR/. In addition, only a very small percentage have a reflectance less than 0.8, indicating that most of the observations are very bright clouds. Because of a relaxed constraint by BTD method, there are still some observations with reflectance less than 0.7. This makes the mean reflectance value for BTD/BT11/slightly smaller than BNR/BT11/. Therefore, the BNR method detects DCCs with more confidence and manages to exclude suspicious DCC pixels with low

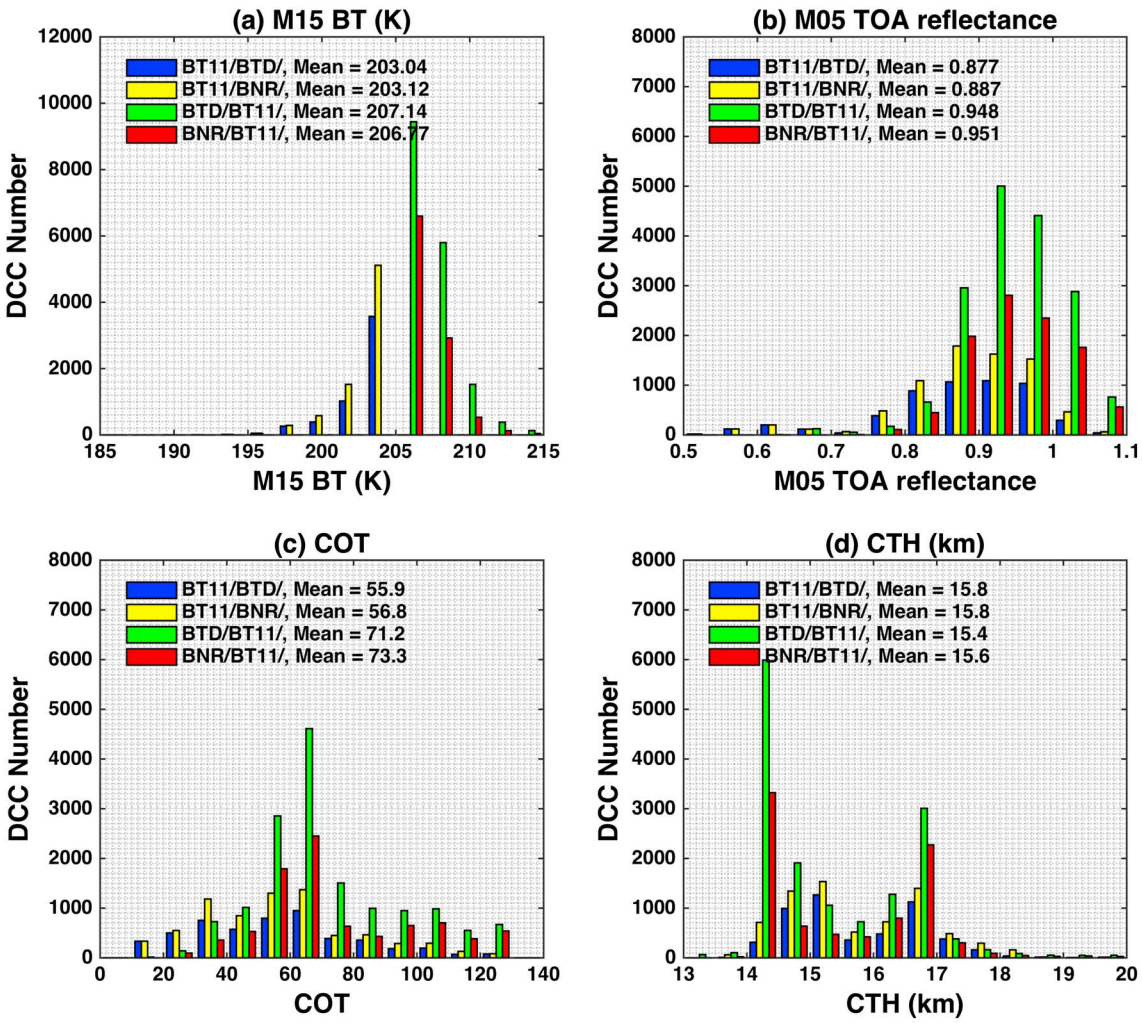

Figure 5. The histograms of (a) M15 brightness temperature (BT; K), (b) M05 top-of-the-atmosphere (TOA) reflectance, (c) cloud optical thickness (COT), and (d) cloud top height (CTH; km) of the four groups of deep convective clouds (DCCs), including those detected by 11-μm brightness temperature (BT11) but not by brightness temperature difference (BTD; BT11/BTD/), by BT11 but not by measurement noise ratio (BNR; BT11/BNR/), by BTD but not by BT11 (BTD/BT11/), and by BNR but not by BT11 (BNR/BT11/). The COT and CTH are from the Visible Infrared Imaging Radiometer Suite (VIIRS) gridded cell-level Cloud Environmental Data Records. The mean values are shown in each panel.

visible reflectance. Similarly, only a small percentage for BTD/BT11/ and BNR/BT11/have COT less than 30, and the mean values are 71.2 and 73.3, respectively; although slightly smaller than the mean values of all detected DCCs (78.7 and 80.2 respectively), the COT values are still much larger than BT11/BTD/and BT11/BNR/. These results indicate that majority of the observations detected by BTD or BNR but missed by BT11 are very thick clouds. Furthermore, with a stricter threshold value, BNR improves on the BTD method by detecting DCCs with more confidence, and excluding areas less likely to have DCCs as the clouds are not bright and thick enough.

Above all, these results indicate that the BTD and BNR methods are superior to the BT11 method in detecting DCCs and BNR further improves on BTD with a stricter threshold value. Basically, DCCs are high, very thick, and very bright clouds. The legacy BT11 method, based on a single threshold value of a window channel, is effective in choosing cold scenes. However, cold scene only ensure that clouds are high as shown in Figure 5d, but not necessarily very thick and bright to become DCCs. As a result, a substantial percentage of the detections are not as bright and probably not DCCs. On the other hand, BTD or BNR detects overshooting clouds with a combination of one very strong WV absorption band and one very clean window band. A cloud must be high and thick to see its WV BT comparable or warmer than the window channel. This ensures that clouds are very high and thick. In addition, by considering the noise contamination and

using a stricter threshold value, BNR further improves the BTD method in detecting DCCs with more confidence and excluding suspicious DCCs, mostly not thick or bright enough.

4. RSB Monitoring Using CrIS-Based DCC Technique

DCCs are bright targets and have nearly Lambertian reflectance. The DCC technique has been widely used for postlaunch calibration and radiometric stability monitoring for the solar reflective spectrum (Bhatt et al., 2014;Doelling et al., 2004 ; Doelling et al., 2011 ; Doelling et al., 2013 ; Fougnie & Bach, 2009 ; Hu et al., 2004 ; Minnis et al., 2008 ; Wang & Cao, 2014, 2015, 2016). In this study, the ADM-adjusted reflectance (the reflectance hereafter) is used for monitoring the VIS/NIR bands, while the TOA reflectance is used for monitoring the SWIR bands. Both the BT11 and BNR methods are applied to process the 2-year data from 1 January 2017 to 31 December 2018 for monitoring the VIIRS RSBs. The comparison results will show improvements of BNR over BT11 in both the statistics and the time series analysis.

4.1. Monthly Statistics Analysis

Figure 6 shows the monthly PDF (probability distribution function) of M05 reflectance (representing VIS/NIR bands) and M08 TOA reflectance (representing SWIR bands) of DCCs detected by the BT11 and BNR methods, for each month of 2017. Statistics for the mean, mode, STD, full width of half maximum (FWHM) of the peak of the monthly PDF, and DCC number (N) are provided. The mean, STD and (Max-Min) of the monthly reflectance mean and mode are shown in black text. To make it simple and clear, the reflectance mean and mode refer to the mean and mode values of the reflectance histogram of DCC samplings. The PDF increment used is 0.005. For VIS/NIR reflectance, higher reflectance mean and mode indicate more confidence in the DCC detection. For all RSBs, smaller STD and FWHM indicate less non-DCC contamination and thus more robust distribution of the DCC reflectance. In addition, smaller STD and (Max-Min) of the monthly mean and mode indicate more invariant and robust time series of the DCC reflectance, which is consistent with the nature of the DCCs.

From Figures 6a and 6b, M05 monthly reflectance mean and mode are over 0.85 for both BT11 and BNR methods, for each month of 2017, indicating DCCs have highly reflective albedos, which is consistent with previous studies (Doelling et al., 2004; Doelling et al., 2011; Doelling et al., 2013; Fougnie & Bach, 2009; Hu et al., 2004; Minnis et al., 2008; Wang & Cao, 2014, 2015, 2016). Note these values are smaller than those shown in Figures 4 and 5 because the ADM adjustment is applied. For each month of 2017, the DCC number for BNR is about half that of BT11, mainly due to the data gaps between CrIS FOVs. When comparing to the BT11 method, for each month of 2017, the statistics for BNR are improved in three ways: (1) The DCC reflectance mean and mode are higher; (2) the STD and FWHM of monthly PDF are smaller, specifically the mean of the monthly STD is significantly reduced by 20.0% from 0.0933 to 0.0746; and (3) the STD and (Max-Min) of the monthly reflectance mean and mode are smaller; that is, the STD of monthly mean values is significantly reduced by 48.5% from 0.68% to 0.35%. These results indicate BNR has a more robust and invariant distribution of DCC reflectance and less variant time series of reflectance mean and mode than the BT11 method. One major reason for the improvement is that BNR is less contaminated with clouds not as bright and thick. This is evidenced by the fact that the monthly PDFs in Figure 6a have longer left tails (less reflective) than those in Figure 6b. Other VIS/NIR bands have the similar behavior as the M05 band.

In Figures 6c and 6d, M08 TOA reflectance is used as an example of SWIR reflectance. Similarly, BNR has a better performance than the BT11 method with a larger mean, smaller STD and FWHM values, and shorter left tail of the monthly PDF of DCC reflectance, for each month of 2017. However, the improvement in BNR over BT11 is slightly less dramatically for SWIR bands, when compared to VIS/NIR bands. For example, the mean of the monthly STD is reduced by 14.9% from 0.0416 to 0.0354, and the STD of the time series of the monthly mean values is significantly reduced by 40% from 0.35% to 0.21%. For both methods, the left tails of M08 TOA reflectance monthly PDFs are not as long as M05, although BNR results in Figure 6d have shorter left tails than BT11 in Figure 6c. Other SWIR bands behave similarly to M08 TOA reflectance. However, the DCC reflectance mean and mode values of SWIR bands are smaller than those of VIS/NIR bands, indicating DCC absorbs some solar radiation in the SWIR spectrum (see also Doelling et al., 2013; Wang & Cao, 2016).

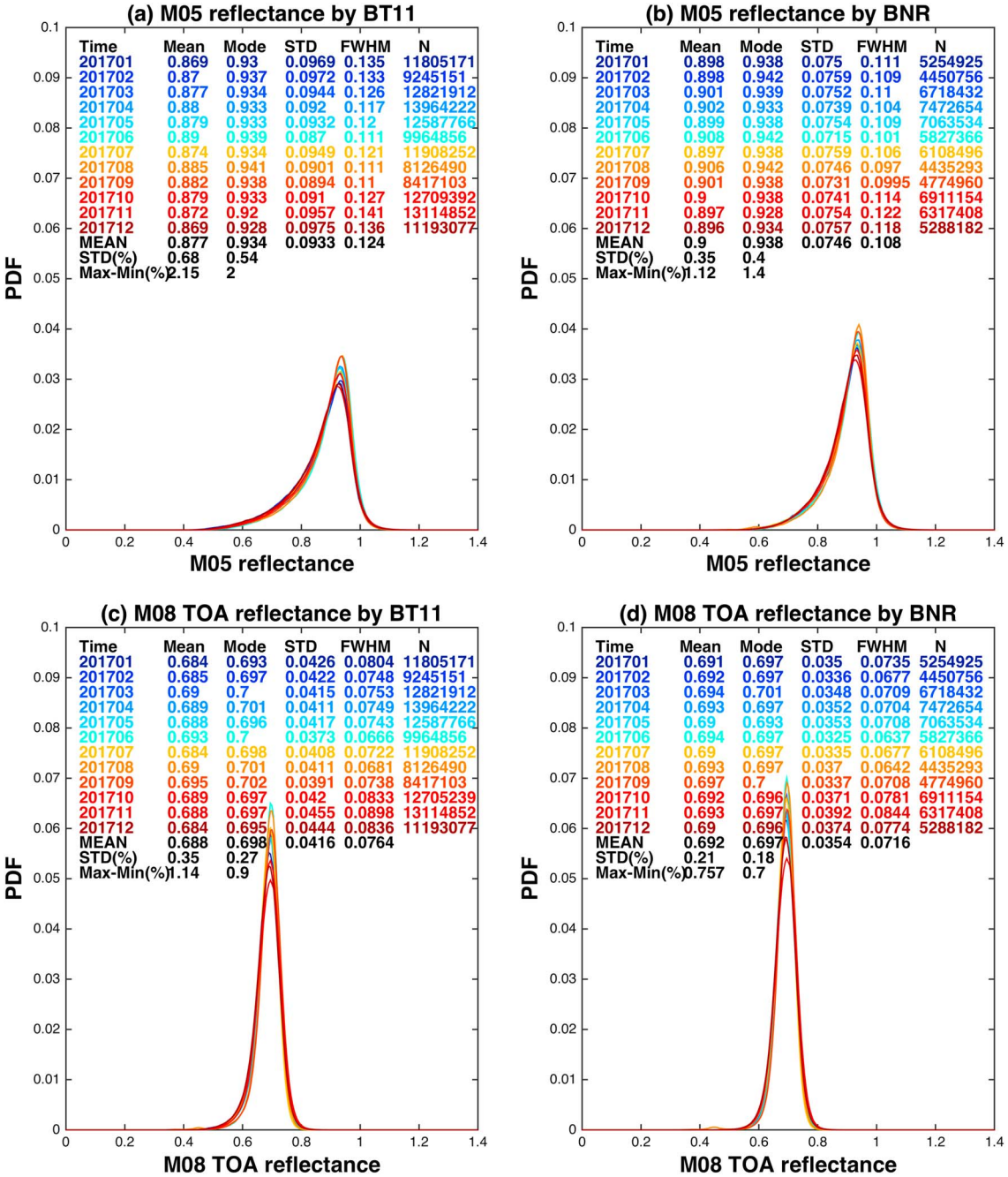

Figure 6. The monthly probability distribution function (PDF) of deep convective clouds detected by the 11-μm brightness temperature (BT11; left) and measurement noise ratio (BNR; right) methods for M05 (upper) and M08 (bottom) for each month of 2017. The monthly mean, mode, standard deviation (STD), full width of half maximum, and deep convective cloud number (*N*) are shown in colors. The mean, STD, and (Max-Min) of monthly statistics are shown in black text. TOA = top of the atmosphere.

4.2. Monthly Time Series Analysis

Figures 7 and 8 show the time series of monthly reflectance mean and mode of the DCCs detected by the BT11 and BNR methods from 1 January 2017 to 31 December 2018, for the VIS/NIR and SWIR bands, respectively, along with the monthly DCC number (in millions). Statistics for the mean, STD, total variation range of (Max-Min), and the trend with a 95% confidence interval of the time series are calculated and summarized for each band. Note that the STD and (Max-Min) are calculated with respect to the monthly mean and mode values, not individual observations, such that they reflect monthly variation. For the VIS/NIR

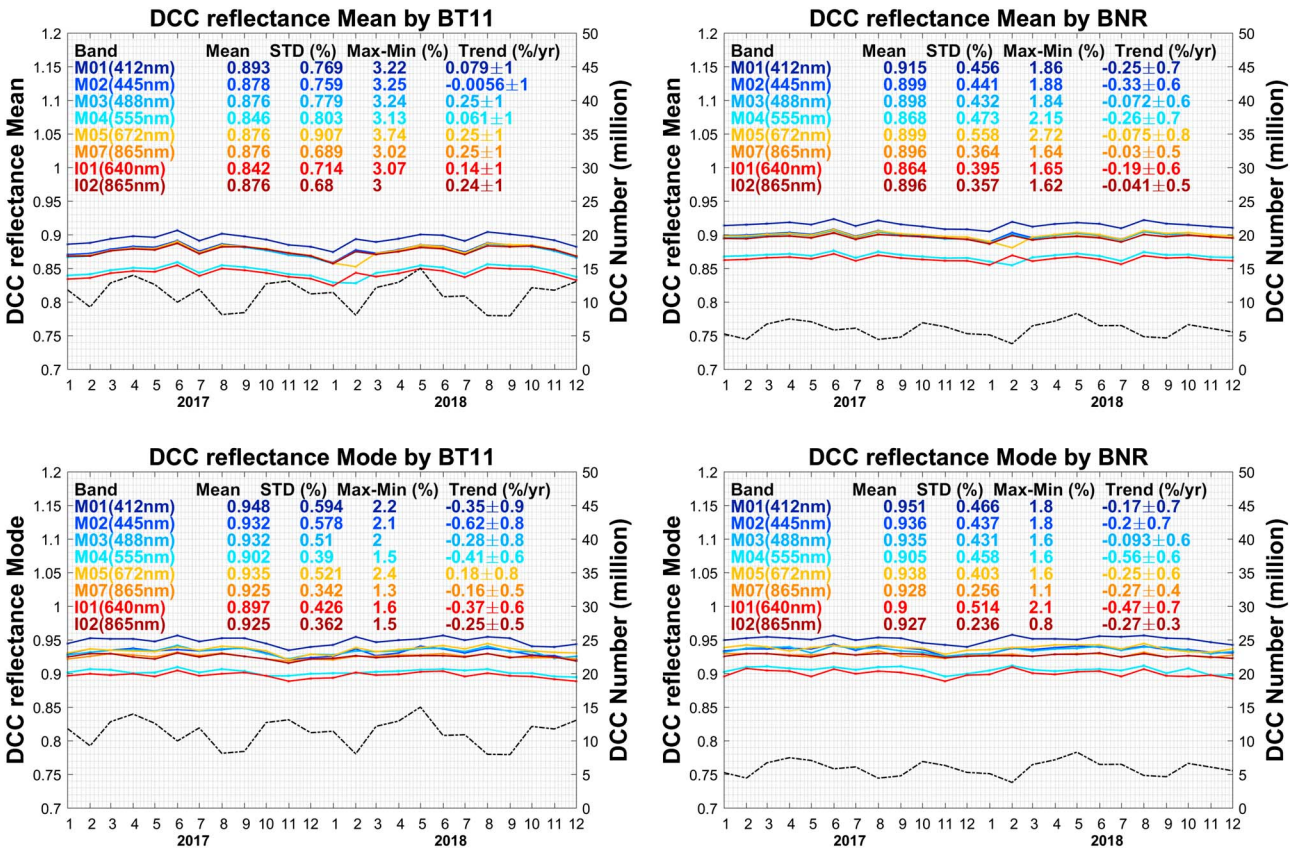

Figure 7. The time series of monthly reflectance mean (top) and mode (bottom) from 1 January 2017 to 31 December 2018 for all VIS/NIR bands for 11-μm brightness temperature (BT11; left) and measurement noise ratio (BNR; right) methods, and deep convective cloud (DCC) number (in millions) is shown in the plots. The statistics for the mean, standard deviation (STD), (Max-Min), and the trend with 95% confidence interval of each time series are shown. VIS = visible; NIR = near-infrared.

bands, the statistics are based on the ADM-adjusted reflectance. As for the SWIR bands, the statistics are based on the TOA reflectance. The time series of the DCC reflectance mean and mode are usually used to monitor the radiometric stabilities of RSBs. The smaller the STD and (Max-Min) of the time series, the more stable and invariant the RSB reflectance. In addition, the trend of the time series often indicates possible degradation of RSBs.

It is important to ensure that the results in Figures 7 and 8 are consistent with those by NOAA VIIRS SDR team (at https://ncc.nesdis.noaa.gov/VIIRS/VSTS.php). For the 2 years from 2017 to 2018, the overall statistics of the mean and STD of the monthly reflectance mean and mode are similar for all VIS/NIR/SWIR bands. The small differences are likely because the results from this study are for the 2 years from 2017 to 2018, while the VIIRS SDR team's results are for the time from 2012 until now. There are also visible differences for individual months; that is, this study shows more stable seasonal variations than the VIIRS SDR team's results. That is likely caused by the different samplings for statistics. The VIIRS SDR team focuses on a region defined as 25°S to 25°N, 150–60°W, a portion of the intertropical convergence zone that is also observed by the current GOES-East and GOES-West satellites with the understanding that the results will benefit the calibration for GEO satellites (Wang & Cao, 2015, 2016), while this study uses observations near equator (25°S to 25°N) of all longitudes.

4.2.1. VIS/NIR Bands Monitoring

Figure 7 shows the monthly time series of DCC reflectance mean and mode from the BT11 and BNR methods. Overall, all VIS/NIR bands follow similar temporal variation in the monthly DCC reflectance mean from both BT11 and BNR methods. Unusual drops are observed for the month of February 2018 for M04 and M05, while all other VIS/NIR bands have a little bit of bumps. These anomalies, as will be shown later, are better identified in the weekly and daily time series in Figures 9 and 10. The reason for these anomalies

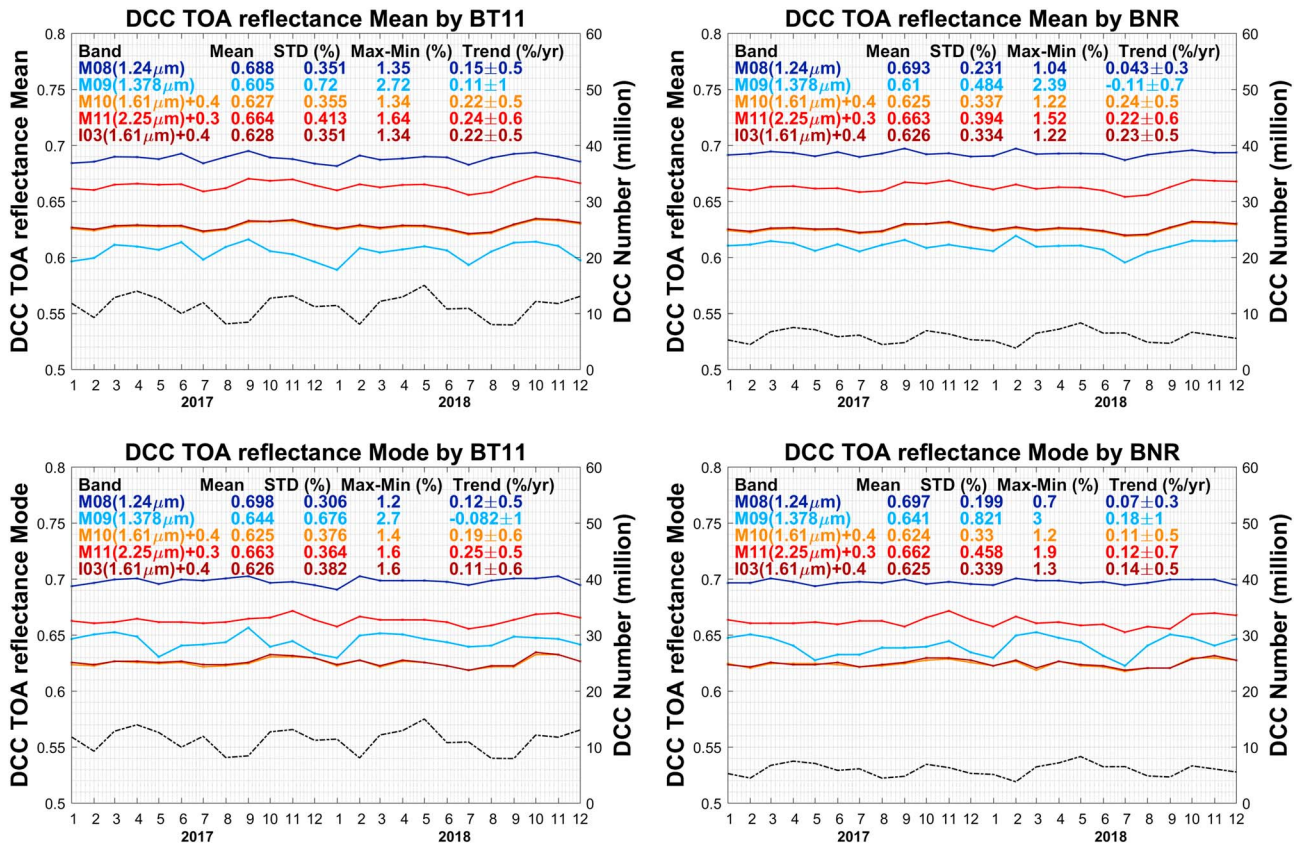

Figure 8. The time series of monthly reflectance mean (top) and mode (bottom) from 1 January 2017 to 31 December 2018 for all shortwave infrared bands for 11-μm brightness temperature (BT11; left) and measurement noise ratio (BNR; right) methods, and deep convective cloud (DCC) number (in millions) is shown in the plots. The statistics for the mean, standard deviation (STD), (Max-Min), and the trend with 95% confidence interval of each time series are shown. TOA = top of the atmosphere.

later was found due to missing solar calibration data for that period. However, the BNR method is less subject to the DCC annual cycle of reflectance mean. For BT11, the annual cycles are shown as a noticeable increase from February to July and a decrease from August to January. However, this is not as visible from BNR. Figure 7 shows that BNR has higher DCC reflectance mean than the BT11 method for all VIS/NIR bands. The statistics of the STD and (Max-Min) of the time series of monthly reflectance mean for BNR is 27–47% smaller than BT11. During the time period from 2017 to 2018, M04 (555 nm) and M05 (672 nm) are more unstable bands than others. BNR has the STD and (Max-Min) of 0.473% and 2.15% for M04 and 0.558% and 2.72% for M05, larger than all other bands and about 27–41% smaller than BT11. BT11 also shows that M04 and M05 have larger STDs than others. Meanwhile, the most stable bands for the entire period are M07 and I02, the two 865-nm bands. BNR has the STD and (Max-Min) of the monthly reflectance mean of 0.364% and 1.64% for M07 and 0.357% and 1.62% for I02, smaller than all other bands and about 45–47% smaller than BT11. These results indicate that, for all VIS/NIR bands, BNR has a significant improvement over BT11, with smaller STD, smaller (Max-Min), and less impact from the annual cycle, all of which indicate more robust and invariant time series of the monthly reflectance mean.

As for the DCC reflectance mode, in most cases, BNR has a better performance than BT11 with larger mean, smaller STD and (Max-Min) values of the monthly time series. However, the improvement in BNR for the mode is not as significant as for the monthly reflectance mean. Section 3.4 shows that the BNR method detects fewer high clouds that are not thick and bright enough. That has a greater effect on the left tails of the PDFs, thus more impact on the mean values than on the modes of the DCC reflectance histograms as shown in Figure 6. As a result, BNR only improves the mean values of the monthly reflectance mode by 0.2–0.4% over BT11 for all VIS/NIR bands. Most of the bands also see improvements in the STD and (Max-Min); the statistics of the STD and (Max-Min) for BNR are up to 47% smaller than BT11. Among all

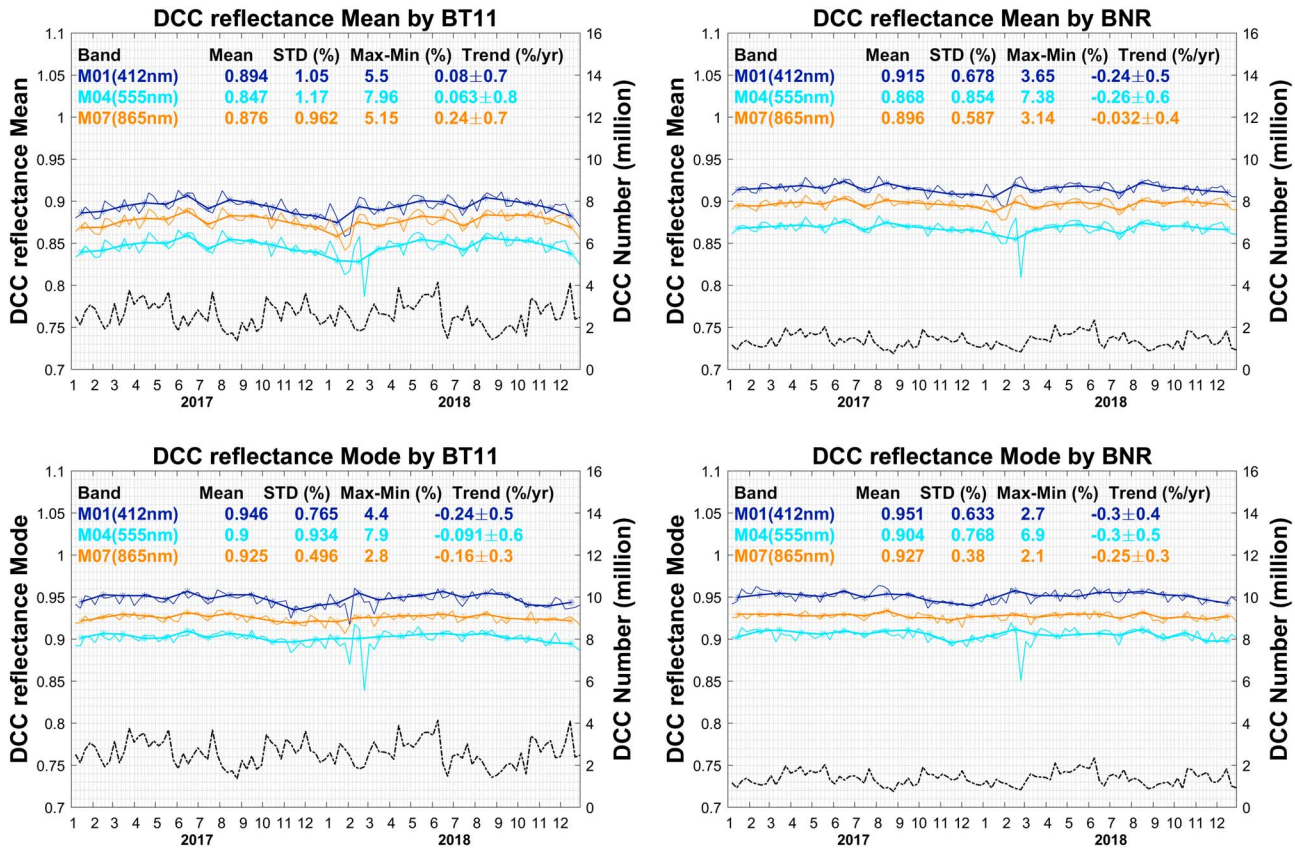

Figure 9. The time series of weekly (solid lines) reflectance mean (top) and mode (bottom) overlaid on the monthly time series (solid lines with stars) from 1 January 2017 to 31 December 2018 for M01, M04, and M07 bands for 11-μm brightness temperature (BT11; left) and measurement noise ratio (BNR; right) methods, and deep convective cloud (DCC) number (in millions) is shown in the plots. The statistics for the mean, standard deviation (STD), (Max-Min), and the trend of the time series are shown at the top of each panel.

VIS/NIR bands, M07 and I02 continue to be the most stable bands for monitoring the monthly modes. BNR has the STD and (Max-Min) of 0.256% and 1.1% for M07 and 0.236% and 0.8% for I02, respectively, and the improvements over BT11 are 15–47%. These results indicate that BNR has much more robust and invariant time series of the monthly reflectance mean and mode for all VIS/NIR bands, when compared to the BT11 method.

For all VIS/NIR bands, the trends of the monthly time series of reflectance mean are within $-0.25 \pm 1\%$ (BT11) and $0.33 \pm 0.6\%$ (BNR), and for the modes are within $-0.62 \pm 0.8\%$ (BT11) and $0.56 \pm 0.7\%$ (BNR), for the 2 years from 2017 to 2018. For example, M02 (445 nm) band has the largest degradation rate of $-0.62 \pm 0.8\%$ for monitoring the monthly modes using the BT11 method; however, the degradation rate is about $-0.2 \pm 0.7\%$ for monitoring the modes using BNR. This is not surprising, because with only 2 years (24 months)' data, the trend of the monthly time series only reflects the seasonal variation. Furthermore, BNR has narrower 95% confidence intervals than BT11, indicating a better performance of BNR over BT11 (see also Figures 8–10).

4.2.2. SWIR Bands Monitoring

From Figure 8, for all SWIR bands, BNR has smaller STD and (Max-Min) of the time series of reflectance mean than the BT11 method, and reductions in percentages are up to 34%. This is also true for the monthly reflectance mode for M08 (1.24 μm), M10 (1.61 μm), and M11 (2.25 μm), but not for M09 (1.378 μm) and M11 (2.25 μm) bands. These results indicate that BNR improves the DCC detection over the BT11 method and yields less variant monthly time series of reflectance mean for all SWIR bands, and the mode in most cases.

For example, M09 (1.378 μm) is an essential band for retrieving convective cloud products of the VIIRS EDRs. The spectral response function of M09 band lies in a WV absorption region. Because DCCs are thick and bright high clouds and there is limited WV above DCC tops, atmospheric absorption is generally

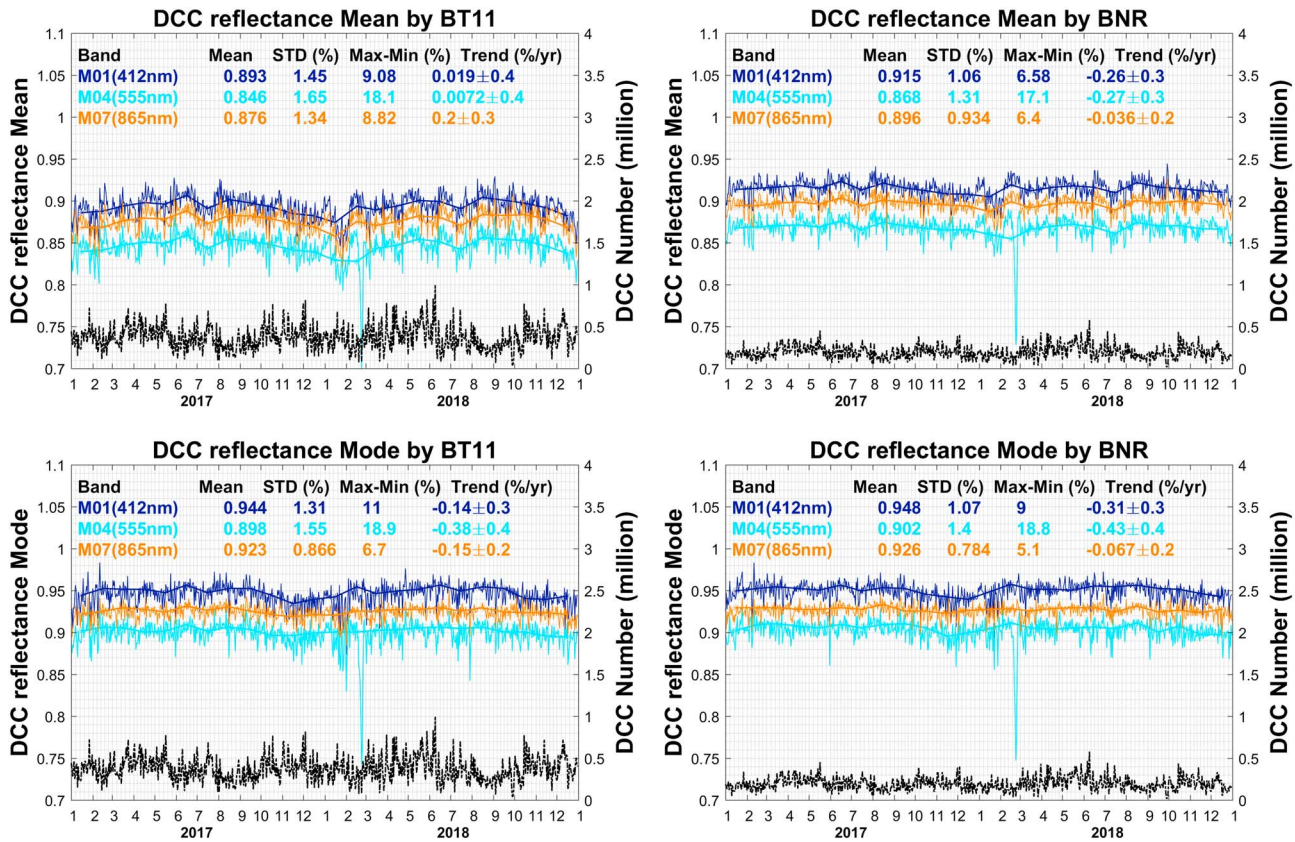

Figure 10. The time series of daily (solid lines) reflectance mean (top) and mode (bottom) overlaid on the monthly time series (solid lines with stars) from 1 January 2017 to 31 December 2018 for M01, M04, and M07 bands for 11-μm brightness temperature (BT11; left) and measurement noise ratio (BNR; right) methods, and deep convective cloud (DCC) number (in millions) is shown in the plots. The statistics for the mean, standard deviation (STD), (Max-Min), and the trend of the time series are shown at the top of each panel.

negligible for M09 band. However, when the DCC detection from the BT11 method is contaminated with high clouds not thick and bright enough, as demonstrated for Hurricane Irma in section 3.4, WV absorption within clouds may have an impact on M09 DCC reflectance. In the left panels of Figure 8, M09 TOA reflectance has a larger monthly variation than other SWIR bands, and the STD and (Max-Min) of the monthly time series are 0.72% and 2.72% for the means and 0.676% and 2.7% for the modes. In the right panels, BNR helps reduce the large monthly variation in M09 band, and the STD and (Max-Min) of the monthly time series are 0.484% and 2.39% for the means and 0.821% and 3% for the modes. Those statistics are changed by −12% to −33% and 11–22% for DCC reflectance mean and mode, respectively, when BNR is compared to the BT11 method. To further study this, the monthly PDFs of the M09 TOA reflectance is examined (not shown). Similar to M05 and M08 shown in Figures 6a and 6c, the PDFs of M09 band have relatively long left tails (less reflective) from the BT11 detection due to the contamination of high clouds not thick and bright enough. And those left tails are more diverse than other bands possibly due to WV absorption in the M09 spectrum. With BNR, most of the contamination is removed, and the left tails are not only substantially shorter, but also more clustered, meaning the PDFs of different months are on top of each other. As a result, the monthly time series of M09 TOA reflectance mean from the BNR method are more stable and temporally invariant than the BT11 method.

Previous studies using BT11 for DCC identification showed annual cycles in the time series of monthly reflectance mean and mode for the SWIR bands (Wang & Cao, 2015, 2016). These annual cycles are partially due to the natural variability of geographical distribution of the DCCs. Compared with Wang and Cao (2015, 2016), who used a portion of the tropical area (25°S to 25°N and 150–60°W), this study is less prone to the DCC natural variability and shows no obvious annual cycles for monitoring the SWIR bands because the

whole tropics are used (25°S to 25°N, 180–180°W). As a result, none of the panels in Figure 8 shows obvious annual cycles.

4.3. Weekly and Daily Time Series Analysis

The time series of DCC reflectance is a useful tool for monitoring the stabilities of RSBs. Previous studies focused on the monthly or semimonthly time series (Wang & Cao, 2014, 2015, 2016). Figures 9 and 10 show the weekly and daily time series of reflectance mean and mode overlaid on the monthly time series from 1 January 2017 to 31 December 2018, for M01 (412 nm), M04 (555 nm), and M07 (865 nm) bands using both BT11 and BNR methods, along with the weekly and daily DCC number (in millions). The statistics of the mean, STD, and (Max-Min) of the weekly and daily time series of reflectance mean and mode are shown at the top of each panel. Note that the STD and (Max-Min) are calculated with respect to the weekly and daily mean and mode values, not individual observations. So they reflect weekly and daily variations, respectively. Three typical spectral bands are shown. M07 band represents the most stable band, while M01 band represents the least stable band for the reflectance mode, among all VIS/NIR M-bands. And M04 band is chosen because both BNR and BT11 have comparably good results in monitoring the monthly reflectance mode, but anomalies are observed in the monthly reflectance mean due to missing calibration data during this period.

From Figures 9 and 10, the time series of the weekly and daily reflectance mean and mode closely follow the monthly time series. And the temporal variations of the three bands look similar, except for the sudden drops occurred in later February 2018 due to missing calibration data for M04 band. This is reasonable because they look at the same clouds. M07 has the smallest STD and (Max-Min) values of the weekly and daily time series, for both BT11 and BNR, which are consistent with the findings from the monthly time series that it is the most stable band of the three. Figures 9 and 10 also show that the daily variation is much larger than the weekly one, both of which are larger than the monthly one. All other RSBs see a similar temporal variation reduction from daily to weekly to monthly. This is true for the reflectance mode as well. For all VIS/NIR bands, BNR has a better performance than BT11, with larger mean, smaller STD, and (Max-Min) values of the weekly and daily time series of reflectance mean and mode (not shown), and the reduction in percentage are up to 39% for the weekly time series, and up to 30% for the daily time series. These results indicate that BNR improves BT11 in monitoring RSBs in higher temporal frequencies. However, the improvements in the weekly and daily time series are not as significant as the monthly time series.

The weekly and daily time series are complementary to the monthly time series because they can be used to pinpoint the anomalies that last much shorter than a month. For example, for daily time series of reflectance mean using BNR method, the reflectance mean value of M04 band on 23 February 2018 is less than 0.73 on Figure 10, a significant drop of 15.8% compared to the mean reflectance (0.868) of the entire period, indicating an anomaly. This drop is more than 10 times of the STD (1.31%) of the daily time series of reflectance mean. This anomaly is also easily identified with a significant drop of more than six times of STD (0.854%) on the weekly time series on Figure 9. Based on the results from Figures 9 and 10, a drop larger than three (weekly) or four (daily) times of its STD indicates a possible anomaly from the weekly and daily time series. The same drop is still somehow visible on the monthly time series on Figure 7, but difficult to confirm the anomaly because of the smooth out of the drop. Weatherhead et al. (2017) provides a good example of how to handle the drifts (or jumps) causing greater uncertainty in long-term satellite records. Therefore, the weekly and daily time series are useful tools to monitor the calibration stabilities of RSBs in higher temporal frequencies. The weekly and daily time series of DCC data sets using BNR method are provided at the SSEC, University of Wisconsin-Madison, website (at http://www.ssec.wisc.edu/dcc/).

While 2 years are too short to study the degradation trend of RSBs. Figures 7, 9, and 10 show that the trends calculated from the 2-year weekly and daily time series are comparable to those from the monthly ones, for the three typical spectral bands M01, M04, and M07. And the trends have narrower 95% confidence intervals for the daily time series than the weekly, and the weekly narrower than the monthly. This indicates the weekly and daily time series maybe be used to monitor the RSB instabilities in long-term trend study.

5. Summary and Future Work

As uniform and stable objects, DCCs are often used to monitor the stabilities of RSB calibrations. Traditionally, the DCCs are identified with the 11 micron BT lower than a threshold, the BT11 method.

BT11 is effective in detecting cold scenes. But cold scene only ensures clouds are high, not necessarily very thick and bright. With one high WV absorption channel (1,419 cm^{-1}) and one window channel (1,231 cm^{-1}) of the CrIS, the BTD, and BNR methods are adopted and applied for the VIIRS DCC identification. To compare the three methods, we looked at the case of Hurricane Irma (2017). Results show the BNR method is superior to either BT11 or BTD method in detecting DCCs because it is less contaminated with high clouds not thick and bright enough. This is enhanced by two additional factors. First, the DCCs must be clustered and mature to be detected by BTD and BNR indices. Second, BNR beats BTD by considering noise contamination and using a stricter threshold value. Only thick and bright clouds have WV BTs comparable or warmer than window channel. The histograms show BNR manages to exclude high clouds not bright and thick enough. Therefore, the BNR method detects DCCs with more confidence, but the overall yield is less.

The methodologies and technical approaches of monitoring the VIIRS RSBs using the DCCs with collocated CrIS measurements are developed. Using the legacy BT11 method as reference, the improvements of BNR for detecting the DCCs and monitoring the RSBs are shown. For VIS/NIR bands, Hu et al.'s ADM (2004) is applied to correct the anisotropy effect in the TOA reflectance. For SWIR bands, the statistics are based on the TOA reflectance. Results show that BNR performs better monitoring the monthly reflectance mean for all VIS/NIR bands, with smaller STD and (Max-Min) values, and less impact from the annual cycle, all of which indicate more robust and invariant time series of the monthly reflectance mean, and reductions of the STD and (Max-Min) in percentage are of 27–47%. As for the DCC reflectance mode, BNR also improves on the BT11 method. However, the improvements are not as significant. This result is reasonable because BNR improves on the left tails more than the modes of the DCC reflectance histograms. For SWIR bands, the reflectance is smaller than VIS/NIR bands due to solar radiation absorption by clouds in SWIR spectrum (see also Doelling et al., 2013; Wang & Cao, 2016). Compared to BT11, BNR has smaller STD and (Max-Min) of the monthly mean for all SWIR bands, and the modes in most cases. These results indicate that BNR has a better performance than BT11 for monitoring all VIS/NIR bands, and in most cases for SWIR bands, because BNR detects more confident DCCs. The improvements in BNR over BT11 are more significant for the reflectance mean than the modes.

More confident DCC detection allows the weekly and daily time series for monitoring the RSBs in high temporal frequencies. Results show the weekly and daily time series closely follow the monthly time series and all RSBs see similar temporal variation reduction from daily to weekly to monthly. And they show similar degradation trends of the RSBs. The weekly and daily time series are complementary to the monthly time series, because they can be used to pinpoint the anomalies lasting much shorter than a month. For example, a drop larger than three (weekly) or four (daily) times of its STD indicates a possible anomaly from the weekly and daily time series. The same drop is sometimes difficult to confirm on the monthly time series because of the smooth out. Therefore, the weekly and daily time series are useful tools to monitor the calibration stabilities of the RSBs. The weekly and daily time series of DCC data sets using the CrIS-based BNR method, for both VIIRS/SNPP and VIIRS/NOAA-20 (former JPSS-1), are provided at the SSEC, University of Wisconsin-Madison, website (at http://www.ssec.wisc.edu/dcc/). This method can be applied to other imager/sounder duos to detect more precise DCCs and monitor the calibration stability of solar reflective spectrum, such as VIIRS with CrIS on the coming additional JPSS series, and the Advanced Geosynchronous Radiation Imager with the Geosynchronous Interferometric InfraRed Sounder on the FengYun-4 GEO satellite series (Yang et al., 2017).

Acknowledgments
This work is partially supported by the JPSS science through the NOAA cooperative agreement program NA15NES4320001, and Chinese Scholarship Council (CSC) for Xinya Gong. The CrIS and VIIRS data used in this study are obtained from NOAA CLASS (www.class.noaa.gov). The views, opinions, and findings contained in this report are those of the authors and should not be construed as an official National Oceanic and Atmospheric Administration's or U.S. government's position, policy, or decision.

References

Ackerman, S. A. (1996). Global satellite observations of negative brightness temperature differences between 11 and 6.7 μm. *Journal of the Atmospheric Sciences*, *53*(19), 2803–2812. https://doi.org/10.1175/1520-0469(1996)053<2803:GSOONB>2.0.CO;2

Ai, Y., Li, J., Shi, W., Schmit, T. J., Cao, C., & Li, W. (2017). Deep convective cloud characterizations from both broadband imager and hyperspectral infrared sounder measurements. *Journal of Geophysical Research: Atmospheres*, *122*, 1700–1712. https://doi.org/10.1002/2016JD025408

Aumann, H. H., DeSouza-Machado, S. G., & Behrangi, A. (2011). Deep convective clouds at the tropopause. *Atmospheric Chemistry and Physics*, *11*(3), 1167–1176. https://doi.org/10.5194/acp-11-1167-2011

Aumann, H. H., Gregorich, D., & De Souza-Machado, S. M. (2006). AIRS observations of deep convective clouds. *Atmospheric and Environmental Remote Sensing Data Processing and Utilization II: Perspective on Calibration/Validation Initiatives and Strategies*. http://doi.org/10.1117/12.681201

Aumann, H. H., & Ruzmaikin, A. (2013). Frequency of deep convective clouds in the tropical zone from 10 years of AIRS data. *Atmospheric Chemistry and Physics*, *13*(21), 10,795–10,806. https://doi.org/10.5194/acp-13-10795-2013

Bedka, K. M., Khlopenkov, K. V., Wang, C., Scarino, B., & Nordeen, M. L. (2018). A 20-Year, Hourly GOES Satellite Derived Deep Convective Cloud Climatology over the Western Hemisphere. *Paper presented at 98th American Meteorological Society Annual Meeting*, Austin, TX, USA

Bhatt, R., Doelling, D. R., Wu, A., Xiong, X., Scarino, B. R., Haney, C. O., & Gopalan, A. (2014). Initial stability assessment of S-NPP VIIRS reflective solar band calibration using invariant desert and deep convective cloud targets. *Remote Sensing*, *6*(4), 2809–2826. https://doi.org/10.3390/rs6042809

Blonski, S., & Cao, C. (2015). Suomi NPP VIIRS reflective solar bands operational calibration reprocessing. *Remote Sensing*, *7*(12), 16,131–16,149. https://doi.org/10.3390/rs71215823

Cao, C., De Luccia, F. J., Xiong, X., Wolfe, R., & Weng, F. (2014). Early on-orbit performance of the visible infrared imaging radiometer suite onboard the Suomi National Polar-Orbiting Partnership (S-NPP) satellite. *IEEE Transactions on Geoscience and Remote Sensing*, *52*(2), 1142–1156. https://doi.org/10.1109/TGRS.2013.2247768

Cao, C., Xiong, J., Blonski, S., Liu, Q., Uprety, S., Shao, X., et al. (2013). Suomi NPP VIIRS sensor data record verification, validation, and long-term performance monitoring. *Journal of Geophysical Research: Atmospheres*, *118*, 11,664–11,678. https://doi.org/10.1002/2013JD020418

Cardema, J. C., Rausch, K. W., Lei, N., Moyer, D. I., & De Luccia, F. J. (2012). Operational calibration of VIIRS reflective solar band sensor data records. *Earth Observing Systems XVII*. http://doi.org/10.1117/12.932221

Chen, L., Hu, X., Xu, N., & Zhang, P. (2013). The application of deep convective clouds in the calibration and response monitoring of the reflective solar bands of FY-3A/MERSI (medium resolution spectral imager). *Remote Sensing*, *5*(12), 6958–6975. https://doi.org/10.3390/rs5126958

Chen, Y., Han, Y., & Weng, F. (2016). Characterization of long-term stability of Suomi NPP cross-track infrared sounder spectral calibration. *IEEE Transactions on Geoscience and Remote Sensing*, *55*(2), 1147–1159. https://doi.org/10.1109/tgrs.2016.2620438

Chen, Y., Han, Y., & Weng, F.(2017). Reprocessing of Suomi NPP CrIS sensor data records and impacts on radiometric and spectral long-term accuracy and stability. *2017 IEEE International Geoscience and Remote Sensing Symposium (IGARSS)*. https://doi.org/10.1109/igarss.2017.8127922

Doelling, D. R., Morstad, D. L., Bhatt, R., & Scarino, B. (2011) Algorithm Theoretical Basis Document (ATBD) for Deep Convective Cloud (DCC) Technique of Calibrating GEO Sensors with Aqua-MODIS for GSICS. Available online:http://gsics.atmos.umd.edu/pub/Development/AtbdCentral/GSICS_ATBD_DCC_NASA_2011_09.pdf (accessed on 24 August 2017)

Doelling, D. R., Morstad, D., Scarino, B. R., Bhatt, R., & Gopalan, A. (2013). The characterization of deep convective clouds as an invariant calibration target and as a visible calibration technique. *IEEE Transactions on Geoscience and Remote Sensing*, *51*(3), 1147–1159. https://doi.org/10.1109/TGRS.2012.2225066

Doelling, D. R., Nguyen, L., & Minnis, P. (2004). On the use of deep convective clouds to calibrate AVHRR data. *Earth Observing Systems IX*. https://doi.org/10.1117/12.560047

Fougnie, B., & Bach, R. (2009). Monitoring of radiometric sensitivity changes of space sensors using deep convective clouds: Operational application to PARASOL. *IEEE Transactions on Geoscience and Remote Sensing*, *47*(3), 851–861. https://doi.org/10.1109/TGRS.2008.2005634

Gong, X., Li, Z., Li, J., Moeller, C. C., Cao, C., Wang, W., & Menzel, W. P. (2018). Intercomparison between VIIRS and CrIS by taking into account the CrIS subpixel cloudiness and viewing geometry. *Journal of Geophysical Research: Atmospheres*, *123*(10), 5335–5345. https://doi.org/10.1029/2017JD027849

Han, Y., Revercomb, H., Cromp, M., Gu, D., Johnson, D., Mooney, D., et al. (2013). Suomi NPP CrIS measurements, sensor data record algorithm, calibration and validation activities, and record data quality. *Journal of Geophysical Research: Atmospheres*, *118*, 12,734–12,748. https://doi.org/10.1002/2013JD020344

Hillger, D., Kopp, T., Lee, T., Lindsey, D., Seaman, C., Miller, S., et al. (2013). First-light imagery from Suomi NPP VIIRS. *Bulletin of the American Meteorological Society*, *94*(7), 1019–1029. https://doi.org/10.1175/BAMS-D-12-00097.1

Hu, Y., Wielicki, B. A., Yang, P., Stackhouse, P. W., Lin, B., & Young, D. F. (2004). Application of deep convective cloud albedo observation to satellite-based study of the terrestrial atmosphere: Monitoring the stability of spaceborne measurements and assessing absorption anomaly. *IEEE Transactions on Geoscience and Remote Sensing*, *42*(11), 2594–2599. https://doi.org/10.1109/tgrs.2004.834765

Li, J., Huang, H. L., Liu, C. Y., Yang, P., Schmit, T. J., Wei, H., et al. (2005). Retrieval of cloud microphysical properties from MODIS and AIRS. *Journal of Applied Meteorology*, *44*(10), 1526–1543. https://doi.org/10.1175/JAM2281.1

Li, J., Liu, C. Y., Huang, H. L., Schmit, T. J., Wu, X., Gurka, J. J., & Menzel, W. P. (2005). Optimal cloud-clearing for AIRS radiances using MODIS. *IEEE Transactions on Geoscience and Remote Sensing*, *43*(6), 1266–1278. https://doi.org/10.1109/tgrs.2005.847795

Li, J., Menzel, W. P., Sun, F., Schmit, T. J., & Gurka, J. (2004). Airs subpixel cloud characterization using modis cloud products. *Journal of Applied Meteorology*, *43*(8), 1083–1094. https://doi.org/10.1175/1520-0450(2004)043<1083:ASCCUM>2.0.CO;2

Li, J., Menzel, W. P., Zhang, W., Sun, F., Schmit, T. J., Gurka, J. J., & Weisz, E. (2004). Synergistic use of modis and airs in a variational retrieval of cloud parameters. *Journal of Applied Meteorology*, *43*(11), 1619–1634. https://doi.org/10.1175/JAM2166.1

Li, J., Wang, P., Han, H., Li, J., & Zheng, J. (2016). On the assimilation of satellite sounder data in cloudy skies in numerical weather prediction models. *Journal of Meteorological Research*, *30*(2), 169–182. https://doi.org/10.1007/s13351-016-5114-2

Menzel, W. P., Schmit, T. J., Zhang, P., & Li, J. (2018). Satellite based atmospheric infrared sounder development and applications. *Bulletin of the American Meteorological Society*, *99*(3), 583–603. https://doi.org/10.1175/BAMS-D-16-0293.1

Minnis, P., Doelling, D. R., Nguyen, L., Miller, W. F., & Chakrapani, V. (2008). Assessment of the visible channel calibrations of the VIRS on TRMM and MODIS on Aqua and Terra. *Journal of Atmospheric and Oceanic Technology*, *25*(3), 385–400. https://doi.org/10.1175/2007JTECHA1021.1

Moeller, C., Tobin, D., & Quinn, G. (2013). S-NPP VIIRS thermal band spectral radiance performance through 18 months of operation on-orbit. *Earth Observing Systems XVIII*. http://doi.org/10.1117/12.2023389

Nagle, F. W., & Holz, R. E. (2009). Computationally efficient methods of collocating satellite, aircraft, and ground observations. *Journal of Atmospheric and Oceanic Technology*, *26*(8), 1585–1595. https://doi.org/10.1175/2008JTECHA1189.1

Rausch, K., Houchin, S., Cardema, J., Moy, G., Haas, E., & Luccia, F. J. D. (2013). Automated calibration of the Suomi National Polar-Orbiting Partnership (S-NPP) Visible Infrared Imaging Radiometer Suite (VIIRS) reflective solar bands. *Journal of Geophysical Research: Atmospheres*, *118*, 13–13,442. https://doi.org/10.1002/2013jd020479

Schmetz, J., Tjemkes, S. A., Gube, M., & Van de Berg, L. (1997). Monitoring deep convection and convective overshooting with METEOSAT. *Advances in Space Research*, *19*(3), 433–441. https://doi.org/10.1016/S0273-1177(97)00051-3

Setvák, M., Lindsey, D. T., Rabin, R. M., Wang, P. K., & Demeterová, A. (2008). Indication of water vapor transport into the lower stratosphere above midlatitude convective storms: Meteosat Second Generation satellite observations and radiative transfer model simulations. *Atmospheric Research*, *89*(1-2), 170–180. https://doi.org/10.1016/j.atmosres.2007.11.031

Setvák, M., Rabin, R. M., & Wang, P. K. (2007). Contribution of the MODIS instrument to observations of deep convective storms and stratospheric moisture detection in GOES and MSG imagery. *Atmospheric Research*, *83*(2-4), 505–518. https://doi.org/10.1016/j.atmosres.2005.09.015

Strow, L. L., Motteler, H., Tobin, D., Revercomb, H., Hannon, S., Buijs, H., et al. (2013). Spectral calibration and validation of the Cross-track Infrared Sounder on the Suomi NPP satellite. *Journal of Geophysical Research: Atmospheres*, *118*, 12,486–12,496. https://doi.org/10.1002/2013JD020480

Sun, J., & Wang, M. (2014). VIIRS reflective solar bands on-orbit calibration and performance: a three-year update. *Earth Observing Missions and Sensors: Development, Implementation, and Characterization III*. http://doi.org/10.1117/12.2068964

Tobin, D., Revercomb, H., Knuteson, R., Taylor, J., Best, F., Borg, L., et al. (2013). Suomi-NPP CrIS radiometric calibration uncertainty. *Journal of Geophysical Research: Atmospheres*, *118*, 10,589–10,600. https://doi.org/10.1002/jgrd.50809

Uprety, S., & Cao, C. (2015). Suomi NPP VIIRS reflective solar band on-orbit radiometric stability and accuracy assessment using desert and Antarctica Dome C sites. *Remote Sensing of Environment*, *166*, 106–115. https://doi.org/10.1016/j.rse.2015.05.021

Uprety, S., Cao, C., Xiong, X., Blonski, S., Wu, A., & Shao, X. (2013). Radiometric intercomparison between Suomi-NPP VIIRS and aqua MODIS reflective solar bands using simultaneous nadir overpass in the low latitudes. *Journal of Atmospheric and Oceanic Technology*, *30*(12), 2720–2736. https://doi.org/10.1175/JTECH-D-13-00071.1

Wang, W., & Cao, C. (2014). Assessing the VIIRS RSB calibration stability using deep convective clouds. *Earth Observing Missions and Sensors: Development, Implementation, and Characterization III*. http://doi.org/10.1117/12.2068434

Wang, L., Han, Y., Jin, X., Chen, Y., & Tremblay, D. A. (2015). Radiometric consistency assessment of hyperspectral infrared sounders. *Atmospheric Measurement Techniques*, *8*(11), 4831–4844. https://doi.org/10.5194/amt-8-4831-2015

Wang, L., Han, Y., Tremblay, D., Weng, F., & Goldberg, M. (2012). Inter-comparison of NPP/CrIS radiances with VIIRS, AIRS, and IASI: a post-launch calibration assessment. *Earth Observing Missions and Sensors: Development, Implementation, and Characterization II*.http://doi.org/10.1117/12.978769

Wang, L., Tremblay, D., Zhang, B., & Han, Y. (2016). Fast and accurate collocation of the visible infrared imaging radiometer suite measurements with Cross-Track Infrared Sounder. *Remote Sensing*, *8*, 76. https://doi.org/10.3390/rs8010076

Wang, L., Tremblay, D. A., Han, Y., Esplin, M., Hagan, D. E., Predina, J., et al. (2013). Geolocation assessment for CrIS sensor data records. *Journal of Geophysical Research: Atmospheres*, *118*, 12,690–12,704. https://doi.org/10.1002/2013JD020376

Wang, L., Zhang, B., Tremblay, D., & Han, Y. (2017). Improved scheme for Cross-track Infrared Sounder geolocation assessment and optimization. *Journal of Geophysical Research: Atmospheres*, *122*, 519–536. https://doi.org/10.1002/2016JD025812

Wang, P., Li, J., Goldberg, M. D., Schmit, T. J., Lim, A. H. N., Li, Z., et al. (2015). Assimilation of thermodynamic information from advanced infrared sounders under partially cloudy skies for regional nwp. *Journal of Geophysical Research: Atmospheres*, *120*, 5469–5484. https://doi.org/10.1002/2014JD022976

Wang, P., Li, J., Li, J., Li, Z., Schmit, T. J., & Bai, W. (2014). Advanced infrared sounder subpixel cloud detection with imagers and its impact on radiance assimilation in NWP. *Geophysical Research Letters*, *41*, 1773–1780. https://doi.org/10.1002/2013GL059067

Wang, P., Li, J., Li, Z., Lim, A. H. N., & Goldberg, M. D. (2017). The impact of cross-track infrared sounder (CrIS) cloud-cleared radiances on Hurricane Joaquin (2015) and Matthew (2016) forecasts. *Journal of Geophysical Research: Atmospheres*, *122*, 13,201–13,218. https://doi.org/10.1002/2017JD027515

Wang, W., & Cao, C. (2015). DCC radiometric sensitivity to spatial resolution, cluster size, and LWIR calibration bias based on VIIRS observations. *Journal of Atmospheric and Oceanic Technology*, *32*(1), 48–60. https://doi.org/10.1175/JTECH-D-14-00024.1

Wang, W., & Cao, C. (2016). Monitoring the NOAA operational VIIRS RSB and DNB calibration stability using monthly and semi-monthly deep convective clouds time series. *Remote Sensing*, *8*(1), 32. https://doi.org/10.3390/rs8010032

Weng, F., Choi, T., Cao, C., & Zhang, B. (2017). Reprocessing of SUOMI NPP VIIRS sensor data records and impacts on environmental applications. *2017 IEEE International Geoscience and Remote Sensing Symposium (IGARSS)*.http://doi.org/10.1109/igarss.2017.8126953

Weatherhead, E. C., Harder, J., Araujo-Pradere, E. A., Bodeker, G., English, J. M., Flynn, L. E., et al. (2017). How long do satellites need to overlap? Evaluation of climate data stability from overlapping satellite records. *Atmospheric Chemistry and Physics*, *17*(24), 15,069–15,093. https://doi.org/10.5194/acp-17-15069-2017

Wolfe, R. E., Lin, G., Nishihama, M., Tewari, K. P., Tilton, J. C., & Isaacman, A. R. (2013). Suomi NPP VIIRS prelaunch and on-orbit geometric calibration and characterization. *Journal of Geophysical Research: Atmospheres*, *118*, 11,508–11,521. https://doi.org/10.1002/jgrd.50873

Wu, A., Xiong, X., Cao, C., & Chiang, K. F. (2016). Assessment of SNPP VIIRS VIS/NIR radiometric calibration stability using Aqua MODIS and invariant surface targets. *IEEE Transactions on Geoscience and Remote Sensing*, *54*(5), 2918–2924. https://doi.org/10.1109/TGRS.2015.2508379

Xiong, X., Butler, J., Chiang, K., Efremova, B., Fulbright, J., Lei, N., et al. (2014). VIIRS on-orbit calibration methodology and performance. *Journal of Geophysical Research: Atmospheres*, *119*, 5065–5078. https://doi.org/10.1002/2013JD020423

Xiong, X., Butler, J., Chiang, K., Efremova, B., Fulbright, J., Lei, N., et al. (2016). Assessment of S-NPP VIIRS on-orbit radiometric calibration and performance. *Remote Sensing*, *8*(2), 84. https://doi.org/10.3390/rs8020084

Yang, J., Zhang, Z., Wei, C., Lu, F., & Guo, Q. (2017). Introducing the new generation of Chinese geostationary weather satellites, FengYun 4 (FY-4). *Bulletin of the American Meteorological Society*, *98*(8), 1637–1658. https://doi.org/10.1175/BAMS-D-16-0065.1

Zavyalov, V. V., Fish, C. S., Bingham, G. E., Esplin, M., Greenman, M., Scott, D., & Han, Y. (2011). Preflight assessment of the cross-track infrared sounder (CrIS) performance. *Sensors, Systems, and Next-Generation Satellites XV*. http://doi.org/10.1117/12.897674

Zavyalov, V., Esplin, M., Scott, D., Esplin, B., Bingham, G., Hoffman, E., et al. (2013). Noise performance of the CrIS instrument. *Journal of Geophysical Research: Atmospheres*, *118*, 13,108–13,120. https://doi.org/10.1002/2013JD020457

Zhou, L., Divakarla, M., & Liu, X. (2016). An overview of the Joint Polar Satellite System (JPSS) science data product calibration and validation. *Remote Sensing*, *8*(2), 139. https://doi.org/10.3390/rs8020139